**Polymer-mediated confined assembly of high-entropy perovskite hydroxide nanocubes for ammonia production and zinc–nitrate battery energy supply**

*Chaofan Liu†, Tian Xie†, Guohao Xue†, Xiaobo Xu, Hele Guo*, Yawen Guan, Tianlu Wang, Ziyuan Rao, Nan Zhang, Tianxi Liu, Claire J. Carmalt, Johan Hofkens, Xiaoqin Zeng and Feili Lai**

C. Liu, T. Xie, X. Xu, Y. Guan, Dr. Z. Rao, Prof. X. Zeng, Dr. F. Lai
State Key Laboratory of Metal Matrix Composites, School of Materials Science and Engineering, Shanghai Jiao Tong University, Shanghai 200240, P. R. China.
E-mail: feililai@sjtu.edu.cn

G. Xue, T. Wang, Prof. N. Zhang, Prof. T. Liu
The Key Laboratory of Synthetic and Biological Colloids, Ministry of Education, School of Chemical and Material Engineering, Jiangnan University, Wuxi, 214122, P. R. China.

Dr. H. Guo, Prof. J. Hofkens, Dr. F. Lai
Department of Chemistry, KU Leuven, Celestijnenlaan 200F, Leuven 3001, Belgium.
E-mail: hele.guo@kuleuven.be; feili.lai@kuleuven.be

Prof. C. J. Carmalt
Department of Chemistry, University College London, London, WC1H0AJ, UK.

†These authors contributed equally to this work.

**Keywords:** high-entropy perovskite hydroxides, electrocatalytic nitrate reduction, polymer-mediated confined assembly, ammonia production, zinc-nitrate battery

High-entropy perovskites, with their compositional diversity and structural tunability, have recently emerged as a versatile platform for electrocatalysis. Among them, high-entropy perovskite hydroxides (HEPHs) offer abundant active sites and flexible electronic structures, yet their controllable synthesis with well-defined morphology remains a major challenge. In this study, we present a polymer-mediated confined assembly strategy that enables the controllable synthesis of nanocubic $Sn(CuMgCoZnNi)(OH)_6$ (HEPH-2). HEPH-2, with highly accessible active sites and a large electrochemically active surface area, delivers outstanding electrocatalytic nitrate reduction to ammonia (eNRA) performance, achieving an ammonia ($NH_3$) yield rate of 9.28 mg $h^{-1}$ $mg^{-1}_{cat.}$ and a high Faradaic efficiency (FE) of 90.06% in alkaline media, significantly outperforming irregular HEPH nanoparticles (HEPH-0) synthesized without polyvinylpyrrolidone. Density functional theory (DFT) calculations reveal that Sn acts as the dominant active site with the strongest $NO_3^-$ adsorption, while the hydrogenation of *NO to *NOH constitutes the rate-determining step. Meanwhile, when used as the cathode material in a zinc-nitrate battery, HEPH-2 demonstrates a high $NH_3$ yield rate (3.70 mg $h^{-1}$ $cm^{-2}$) and a high FE value (94.21%). This work introduces a simple yet effective strategy for engineering well-defined perovskite hydroxides, demonstrating their potential as next-generation materials for sustainable ammonia production and energy conversion.

## 1. Introduction

Ammonia ($NH_3$), a cornerstone of the nitrogen cycle and modern industry, is essential for producing fertilizers, explosives, and plastics.[1] Nitrogen fixation, which converts atmospheric nitrogen into bioavailable forms, ranks among nature's most essential processes after photosynthesis. However, its limited natural rate cannot meet the ever-increasing demand for ammonia-based resources. The Haber-Bosch process, developed over a century ago, revolutionized $NH_3$ production, but its reliance on extreme conditions, high energy consumption, and environmental impact underscores the need for sustainable alternatives.[2] Electrocatalytic $N_2$ fixation represents a promising alternative, as it operates under ambient conditions, utilizes water as the proton source, and can be directly powered by renewable electricity.[3] Its simplicity, efficiency, and

environmental benefits make it a key area of research for providing a cleaner, more sustainable pathway to meet global demands and reduce the ecological footprint. However, the challenge lies in the exceptional stability of $N_2$, arising from its strong N≡N bond (941 kJ $mol^{-1}$), unfavorable electronic structure, and poor solubility in aqueous electrolytes, all of which impede activation and dissociation.[3d, 4] As an alternative, electrocatalytic nitrate ($NO_3^-$) reduction to ammonia (eNRA) has gained attention due to the high solubility of nitrate and the relatively weak N=O bond.[5] This approach not only enhances $NH_3$ production and Faradaic efficiency (FE) but also addresses environmental concerns by utilizing nitrate ions, common pollutants in wastewater, as a feedstock.[1f, 6]

High-entropy materials (HEMs) have recently emerged as promising candidates for electrocatalysis owing to their abundant active sites, complex electronic configurations, and disordered elemental arrangements.[7] Among them, high-entropy perovskites (oxides and hydroxides) are particularly attractive owing to their compositional tunability and robust structural stability.[8] Nevertheless, conventional perovskite oxides often suffer from limited surface area and relatively low catalytic activity, largely as a result of their bulk morphology and high crystallization temperatures required for synthesis.[9] By contrast, perovskite hydroxides represent a distinctive class of $ReO_3$-type structures that can be readily synthesized on a large scale through simple co-precipitation or hydrothermal methods.[9] Their mild synthesis conditions facilitate morphological control and enable the incorporation of multiple elements, giving rise to high-entropy perovskite hydroxides (HEPHs). Such structural and compositional flexibility enhances electronic coupling among different cations, thereby improving charge transfer during electrocatalytic reactions and boosting $NH_3$ yield and FE in eNRA. Moreover, under alkaline conditions, HEPHs combine excellent chemical stability with accelerated nitrate reduction kinetics, effectively suppressing catalyst degradation and synergistically improving overall efficiency.[10]

Herein, nanocubic $Sn(CuMgCoZnNi)(OH)_6$ HEPHs were successfully synthesized on a gram scale using a polymer-mediated confined assembly method. The uniform spatial distribution and high density of oxygen-/nitrogen-containing groups along the

polyvinylpyrrolidone (PVP) chains serve as effective nucleation sites, enabling controlled growth of multi-component perovskite hydroxides with diverse structures and high-entropy characteristics. By tuning the PVP content, the morphology and composition of HEPHs can be effectively regulated, thereby optimizing their overall electrocatalytic activity. Among them, HEPH-2 (synthesized with a PVP mass fraction of 10%) demonstrates remarkable electrocatalytic performance for the eNRA, achieving an impressive $NH_3$ yield rate of 9.28 mg $h^{-1}$ $mg^{-1}_{cat.}$ and a high FE of 90.06%, which outperforms irregular HEPH nanoparticles synthesized without PVP. More importantly, density functional theory (DFT) calculations of $NO_3^-$ adsorption energies reveal that Sn sites in HEPHs exhibit favorable thermodynamic performance for nitrate reduction. Additionally, when HEPH-2 is employed as the cathode material in a zinc-nitrate battery, the system demonstrates a high $NH_3$ production rate (3.70 mg $h^{-1}$ $cm^{-2}$) and a high FE value (94.21%). This study presents a scalable strategy to construct structurally engineered HEPHs with enhanced stability and activity, providing new insights for high-performance electrocatalyst design.

## 2. Results and discussion

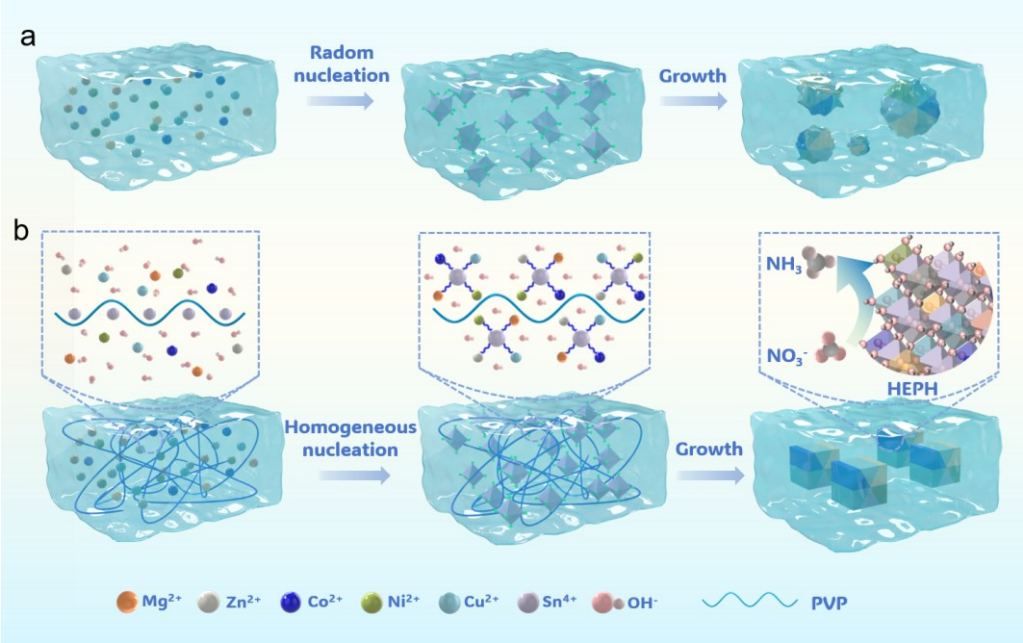


**Figure 1.** Schematic illustration for the preparation of HEPH by the coprecipitation method (a) without and (b) with the aid of PVP.

**Figure 1** schematically illustrates the different formation pathways of HEPHs

obtained by conventional co-precipitation and PVP-mediated confined assembly. As shown in Figure 1a, the traditional co-precipitation method proceeds through random nucleation and uncontrolled growth of metal hydroxide species, which ultimately results in irregularly shaped and agglomerated HEPH nanoparticles (HEPH-0). In contrast, when PVP molecules are introduced (Figure 1b), the abundant polar groups along the polymer chains act as coordination and anchoring sites for the metal cations, guiding their homogeneous dispersion within the polymer network. This confined microenvironment promotes uniform nucleation and restricts uncontrolled growth, thereby driving the formation of highly ordered nanocubic $Sn(CuMgCoZnNi)(OH)_6$ HEPHs with well-defined morphology and improved structural stability. Moreover, this strategy successfully enables the gram-scale synthesis of HEPHs (Figure S1). Three samples, HEPH-0, HEPH-1, and HEPH-2, were synthesized with different PVP mass fractions of 0%, 5%, and 10%, respectively. The X-ray diffraction (XRD) patterns of HEPH-0, HEPH-1, and HEPH-2 reveal distinct diffraction peaks at 2θ values of approximately 20.0°, 23.0°, 32.8°, 36.9°, 38.3°, 40.5°, 43.8°, 47.1°, 51.6°, 52.9°, 58.3°, 62.0°, 68.4°, 72.0°, 73.2°, and 77.8°. These peaks correspond to the (111), (200), (220), (310), (311), (222), (321), (400), (331), (420), (422), (511), (440), (531), (442), and (620) crystal planes of HEPH, aligning with the orthorhombic perovskite structure of $SnCo(OH)_6$ (JCPDS card No. 13-0356, **Figure 2**a). This structural similarity suggests that $Cu^{2+}$, $Mg^{2+}$, $Co^{2+}$, $Zn^{2+}$, and $Ni^{2+}$ ions are incorporated into the lattice of $SnCo(OH)_6$-type perovskite hydroxide, forming a high-entropy $Sn(CuMgCoZnNi)(OH)_6$ solid solution. Figure 2b illustrates the ideal framework of $Sn(CuMgCoZnNi)(OH)_6$. The B-site cations ($Cu^{2+}$, $Mg^{2+}$, $Co^{2+}$, $Zn^{2+}$, and $Ni^{2+}$) are octahedrally coordinated by six hydroxyl groups and located at the centers of corner-sharing $BO_6$ octahedra, forming a three-dimensional framework. The larger A-site cation $Sn^{4+}$ resides in the cuboctahedral cavity created by the surrounding octahedra, exhibiting a 12-fold coordination environment.

Scanning electron microscopy (SEM) analysis shows that HEPH-2 possesses a well-defined nanocubic morphology with a narrow size distribution (Figure 2c). By contrast, HEPH-0 displays a disordered and severely agglomerated structure (Figure S2), while

HEPH-1 shows agglomerated clusters of partially formed nanocubes with irregular sizes (Figure S3), representing an intermediate morphology between the disordered HEPH-0 and the well-defined cubic HEPH-2. These results highlight the critical role of PVP in directing nucleation and growth, thereby enabling the formation of uniform nanocubic architectures. High-resolution transmission electron microscopy (HRTEM) image further reveals clear lattice fringes of 0.225 nm in HEPH-2, corresponding to the (222) planes of the cubic phase (Figure 2d). In addition, energy-dispersive X-ray spectroscopy (EDS) elemental mappings demonstrate the homogeneous distributions of Sn, Mg, Co, Ni, Cu, Zn, and O throughout HEPH-2 (Figure 2e), further providing strong evidence for the successful formation of a single-phase $Sn(CuMgCoZnNi)(OH)_6$ solid solution.

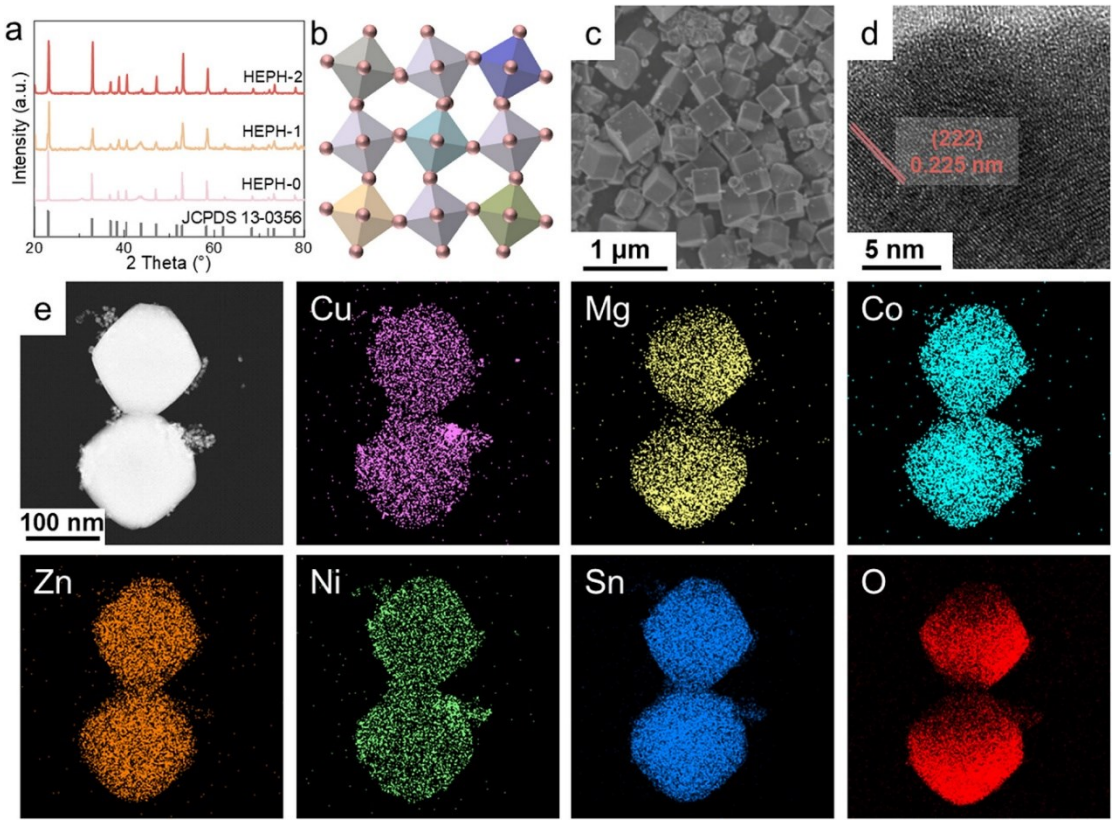


**Figure 2.** (a) XRD patterns of HEPH samples prepared with different PVP contents. (b) Schematic presentation of the HEPH structure: the orange, silver, bright blue, green, light blue, gray-purple, and pink spheres represent Mg, Zn, Co, Ni, Cu, Sn atoms, and OH- group, respectively. (c) SEM, (d) HRTEM, and (e) HAADF-STEM images and corresponding EDS elemental mappings of HEPH-2.

X-ray photoelectron spectroscopy (XPS) was employed to analyze the chemical compositions and oxidation states of HEPH-2 and HEPH-0. As depicted in **Figure 3**a, the full survey spectra of both samples clearly reveal the presence of Sn, Cu, Mg, Co, Zn, Ni, and O elements. The high-resolution Cu 2p spectra of HEPH-0 and HEPH-2 are presented in Figure 3b. Each spectrum can be deconvoluted into six distinct peaks, corresponding to $Cu^{2+}$ $2p_{3/2}$ (937.6 eV), $Cu^{2+}$ $2p_{1/2}$ (955.5 eV), $Cu^{+}$ $2p_{3/2}$ (933.0 eV), $Cu^{+}$ $2p_{1/2}$ (952.6 eV), and two satellite peaks.[11] The high-resolution Mg 1s spectra of HEPH-2 and HEPH-0 (Figure 3c) indicate that Mg predominantly exists in the +2 oxidation state, with a characteristic binding energy of 1303.8 eV.[12] The high-resolution Co 2p spectrum of HEPH-2 can be deconvoluted into six peaks, corresponding to $Co^{3+}$ $2p_{3/2}$ (781.0 eV), $Co^{3+}$ $2p_{1/2}$ (796.8 eV), $Co^{2+}$ $2p_{3/2}$ (785.2 eV), $Co^{2+}$ $2p_{1/2}$ (801.0 eV), and two satellite peaks (Figure 3d).[13] Moreover, the high-resolution Zn 2p spectra of HEPH-2 and HEPH-0 exhibit characteristic spin-orbit splitting, with peaks at 1044.9 eV (Zn $2p_{1/2}$) and 1021.8 eV (Zn $2p_{3/2}$), corresponding to $Zn^{2+}$ species (Figure 3e).[14] High-resolution Sn 3d spectrum of HEPH-2 can be deconvoluted into six peaks, which are related to the $Sn^{0}$ $3d_{5/2}$ (484.5 eV), $Sn^{2+}$ $3d_{5/2}$ (486.5 eV), $Sn^{4+}$ $3d_{5/2}$ (487.9 eV), $Sn^{0}$ $3d_{3/2}$ (492.9 eV), $Sn^{2+}$ $3d_{3/2}$ (494.9 eV), and $Sn^{4+}$ $3d_{3/2}$ (496.5 eV), respectively (Figure 3f).[15]

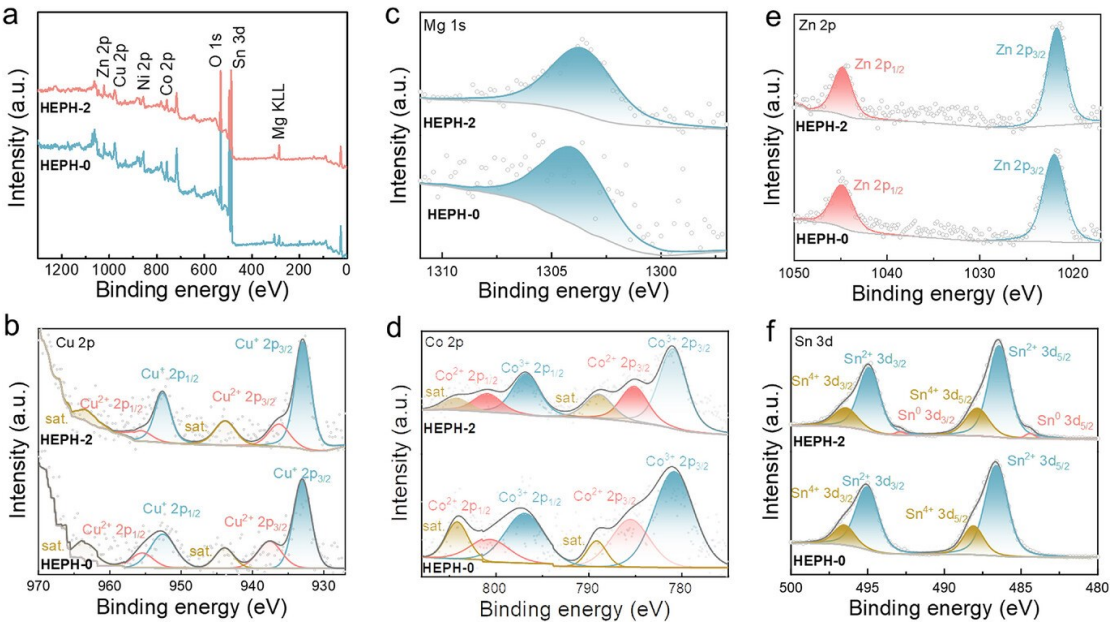


**Figure 3.** XPS survey: a) full, b) Cu 2p, c) Mg 1s, d) Co 2p, e) Zn 2p, and f) Sn 3d spectra of HEPH-2 and HEPH-0 catalysts.

To evaluate the eNRA performance of HEPH-2, HEPH-1, and HEPH-0, comprehensive electrochemical tests were carried out in a conventional three-electrode system using 1 M KOH electrolyte containing 0.1 M $KNO_3$. As shown in the linear sweep voltammetry (LSV) curves (**Figure 4**a and Figures S4–S5), all catalysts exhibit markedly higher current densities in the $KNO_3$-containing electrolyte compared to the $KNO_3$-free electrolyte, confirming the occurrence of nitrate electroreduction. Quantitative assessment of $NH_3$ formation was performed by chronoamperometry at potentials from −0.3 to −0.8 V vs. RHE for 1 h, followed by ultraviolet–visible (UV-Vis) absorption spectroscopy based on the calibration curves correlating absorbance with $NH_3$ concentration (Figure S6). The HEPH-2 catalyst exhibits a remarkable $NH_3$ yield rate of 9.28 mg $h^{-1}$ $mg^{-1}_{cat.}$ and a maximum FE value of 90.06% at -0.4 V vs. RHE, significantly outperforming HEPH-1 (7.64 mg $h^{-1}$ $mg^{-1}_{cat.}$ and 84.0%) and HEPH-0 catalyst (6.10 mg $h^{-1}$ $mg^{-1}_{cat.}$ and 59.7%), as shown in Figure 4b-4c. Additionally, Figure 4d reveals that the $NH_3$ yield rate and FE value exhibit minor fluctuations and remain stable across multiple cycles, highlighting the exceptional electrocatalytic stability of HEPH-2 for potential practical applications. The long-term chronoamperometry confirms stable current density for at least 20 h (Figure 4e), highlighting the excellent durability of HEPH-2. To further assess its structural robustness, post-reaction characterizations were performed. As shown in Figure S7, the XRD pattern of HEPH-2 remains nearly identical to that before the reaction, confirming structural integrity during the eNRA process. SEM image (Figure S8) reveals that the nanocubic morphology is well preserved, while EDS elemental mappings (Figure S9) confirm the uniform elemental distributions of Sn, Mg, Co, Ni, Cu, Zn, and O after catalysis. These results collectively demonstrate the outstanding structural and compositional stabilities of HEPH-2 during long-term operation.

To unambiguously verify the nitrogen source of the produced $NH_3$, isotope-labeling experiments were carried out using electrolytes containing 0.1 M $K^{15}NO_3$ and $K^{14}NO_3$. The $^1H$ NMR spectra of the post-reaction electrolytes clearly distinguish between $^{15}NH_4^+$ and $^{14}NH_4^+$ products: in the case of $K^{15}NO_3$, a characteristic doublet splitting is observed at 6.92 and 7.05 ppm, while for $K^{14}NO_3$, a typical triplet signal appears at

6.90, 6.99, and 7.07 ppm (Figure 4f). These results provide direct spectroscopic evidence that the detected $NH_3$ originates exclusively from the electroreduction of nitrate rather than from external contamination or experimental artifacts. Furthermore, when benchmarked against representative state-of-the-art eNRA catalysts reported in the literature (Table S1), HEPH-2 exhibits comparable or even superior activity. The combination of high yield rate and excellent FE therefore positions HEPH-2 among the most efficient and reliable electrocatalysts reported to date for the nitrate-to-ammonia conversion.

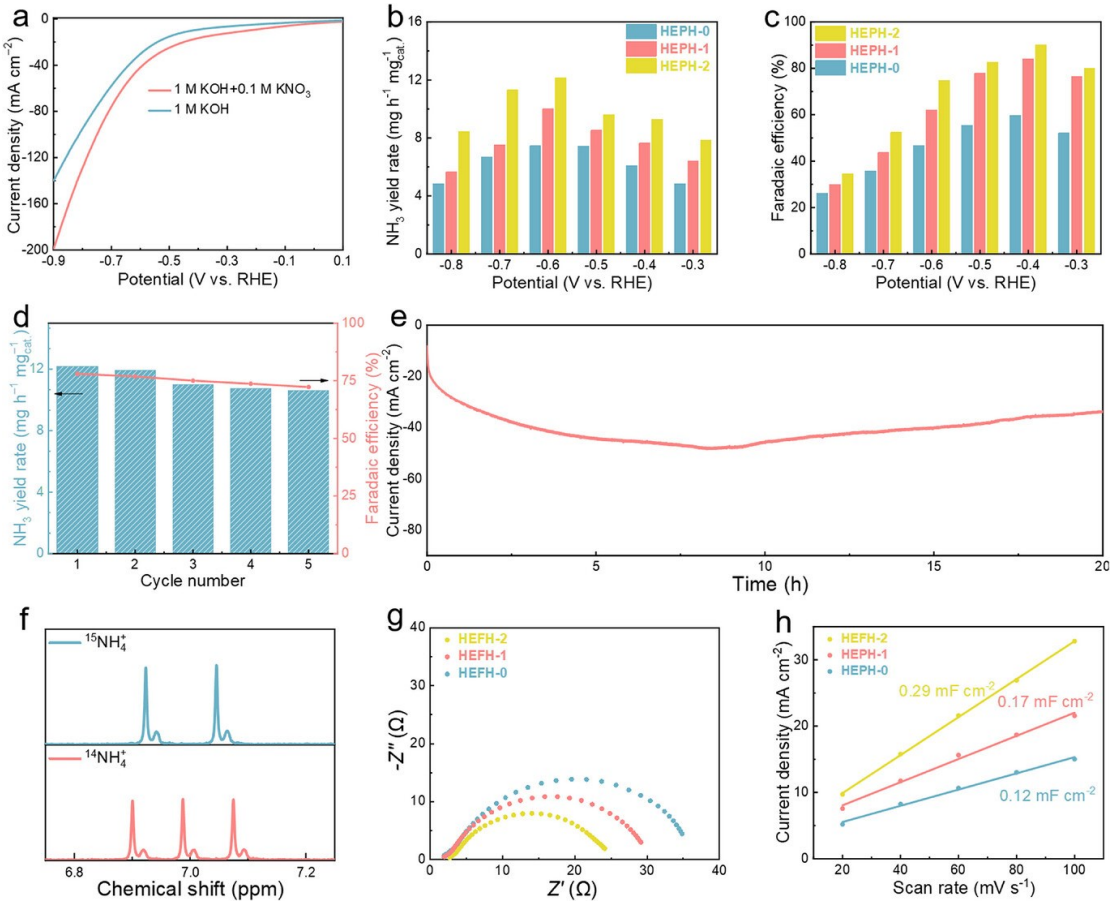


**Figure 4.** a) LSV curves for HEPH-2 in 1 M KOH electrolyte with and without $KNO_3$. b) $NH_3$ yield rates and c) FEs of HEPH-2, HEPH-1, and HEPH-0 under different potentials. d) $NH_3$ yield rates and FE values of HEPH-2 at −0.6 V vs. RHE for 5 cycles. e) Long-term stability test of HEPH-2 catalyst at −0.6 V vs. RHE in 1 M KOH with 0.1 M $KNO_3$ electrolyte. f) $^1H$ NMR spectra of electrolytes prepared with $K^{15}NO_3$ and $K^{14}NO_3$ as nitrogen sources, respectively. g) Nyquist plots of HEPH-2, HEPH-1, and HEPH-0 catalysts. h) The $C_{dl}$ values of HEPH-2, HEPH-1, and HEPH-0 catalysts.

For electrocatalysts, faster charge transfer and larger active surface areas are crucial

for accelerating reaction kinetics. To probe these factors, electrochemical impedance spectroscopy (EIS) and electrochemically active surface area (ECSA) measurements were performed on the HEPH catalysts. As shown in Figure 4g, the charge transfer resistance values of HEPH-2, HEPH-1, and HEPH-0 are determined to be 25, 30, and 36 Ω, respectively, indicating the most efficient charge transport in HEPH-2. The ECSA is further evaluated by recording capacitive currents at scan rates of 20-100 mV $s^{-1}$ within non-Faradaic potential regions (Figures S10–S12). Linear fitting of the current response (Figure 4h) reveals that HEPH-2 possesses a markedly higher double-layer capacitance ($C_{dl}$) of 0.29 mF $cm^{-2}$ compared to HEPH-1 (0.17 mF $cm^{-2}$) and HEPH-0 (0.12 mF $cm^{-2}$). These results underscore the advantages of HEPH-2, where the well-defined nanocubic architecture provides a larger ECSA, reduced charge-transfer resistance, and more favorable redox potential, collectively accounting for its superior eNRA performance relative to HEPH-0 and HEPH-1.

To gain mechanistic insight into the eNRA process on HEPH-2, *in situ* Raman spectroscopy measurements were performed under various operating potentials (**Figure 5**a). In the Raman spectrum of HEPH-2, the characteristic peak at 600 $cm^{-1}$ is attributed to the bending vibration mode of the M-OH bond,[16] while the characteristic peaks at around 800 $cm^{-1}$ are associated with the vibration of the Sn-O bond, confirming the integrity of the perovskite hydroxide framework.[17] A band at 1060 $cm^{-1}$, assigned to adsorbed $NO_3^-$.[18] As the potential shifts negatively from 0 to −0.9 V, the absorption band at 1190 $cm^{-1}$ (corresponding to the N-O antisymmetric stretching vibration of $NO_2^-$) gradually intensifies, indicating the reduction of $NO_3^-$ to $NO_2^-$[18]. Notably, distinct Raman features appear around 1600 $cm^{-1}$, which can be attributed to -$NH_2$ species[19], providing direct evidence that $NO_3^-$ undergoes stepwise deoxygenation followed by successive hydrogenation, ultimately yielding $NH_3$.[20]

To elucidate the reaction pathways and mechanisms of $NO_3^-$ reduction on the HEPH-2 surface, density functional theory (DFT) calculations were further performed. Based on the optimized model, the adsorption energies of $NO_3^-$ species at different sites were calculated theoretically (Figure 5b and Figures S13-S19). The results show that the Sn site exhibits the strongest affinity for $NO_3^-$, pinpointing it as the dominant active center

for the eNRA. Figure 5c depicts the free-energy profile for nitrate electroreduction on the Sn site of HEPH-2, highlighting a multi-step pathway through sequentially adsorbed intermediates (*$NO_3$, *$NO_2$, *NO, *NOH, *NHOH, *NH, and *$NH_2$). The initial adsorption of $NO_3^-$ onto the Sn site is strongly exergonic, consistent with the high adsorption affinity predicted by DFT and indicative of spontaneous surface activation. The subsequent reduction from *$NO_3$ to *$NO_2$ is thermodynamically downhill, facilitating rapid conversion at the initial stage. The conversion from *$NO_2$ to *NO exhibits a modest uphill free-energy change but proceeds with a low kinetic barrier, suggesting that this elementary step is thermodynamically less favorable yet readily activated under applied bias. The pathway then enters a critical hydrogenation stage, where the conversion of *NO to *NOH involves a significant uphill free-energy change, pinpointing it as the potential-determining step (PDS). This barrier originates from the requirement to weaken the N-O bond while simultaneously accommodating proton-electron transfer, a common bottleneck in nitrate-to-ammonia conversion.[18] Once this transition is overcome, later hydrogenation steps (*NOH → *NHOH → *NH → *$NH_2$ → $NH_3$) are increasingly downhill, driving the reaction irreversibly toward $NH_3$ formation. These insights not only confirm the role of Sn as the dominant active center for nitrate binding and activation but also provide a mechanistic rationale for designing improved HEPH catalysts with optimized hydrogenation kinetics.

The zinc-nitrate (Zn-$NO_3^-$) battery represents an emerging energy conversion system capable of simultaneously delivering clean electricity and upgrading $NO_3^-$ from wastewater into high-value $NH_3$.[21] To demonstrate its application potential, a proof-of-concept Zn-$NO_3^-$ battery was assembled using HEPH-2 as the cathode catalyst and zinc foil as the anode. Figure S20 shows that the self-assembled battery maintains a stable open-circuit potential (OCP) of 1.34 V (vs. $Zn^{2+}$/Zn). Figure 5d displays the typical discharge polarization and power density curve of the Zn-$NO_3^-$ battery, exhibiting a high current density of 10 mA $cm^{-2}$ at 0.248 V. The peak power density of the Zn-$NO_3^-$ battery reaches 2.75 mW $cm^{-2}$ at a voltage of 0.15 V. As depicted in Figure 5e, the potential of the Zn-$NO_3^-$ battery remains stable during discharge at various current densities (0.2, 0.5, 1, 1.5, and 2 mA $cm^{-2}$). Notably, the system demonstrates

specific capacity of 498 mAh $g^{-1}$ at the current density of 10 mA $cm^{-2}$ (Figure S21). Additionally, the HEPH-2 cell achieves a maximum FE of 94.21% at 25 mA $cm^{-2}$, which corresponds to an $NH_3$ production rate as high as 3.70 mg $h^{-1}$ $cm^{-2}$ (Figure 5f). Moreover, the assembled Zn-$NO_3^-$ battery exhibits highly stable charge-discharge behavior and excellent cycling durability over 20 h of continuous operation at 1 mA $cm^{-2}$ (Figure S22). These results highlight the potential of this catalyst for Zn-$NO_3^-$ battery applications.

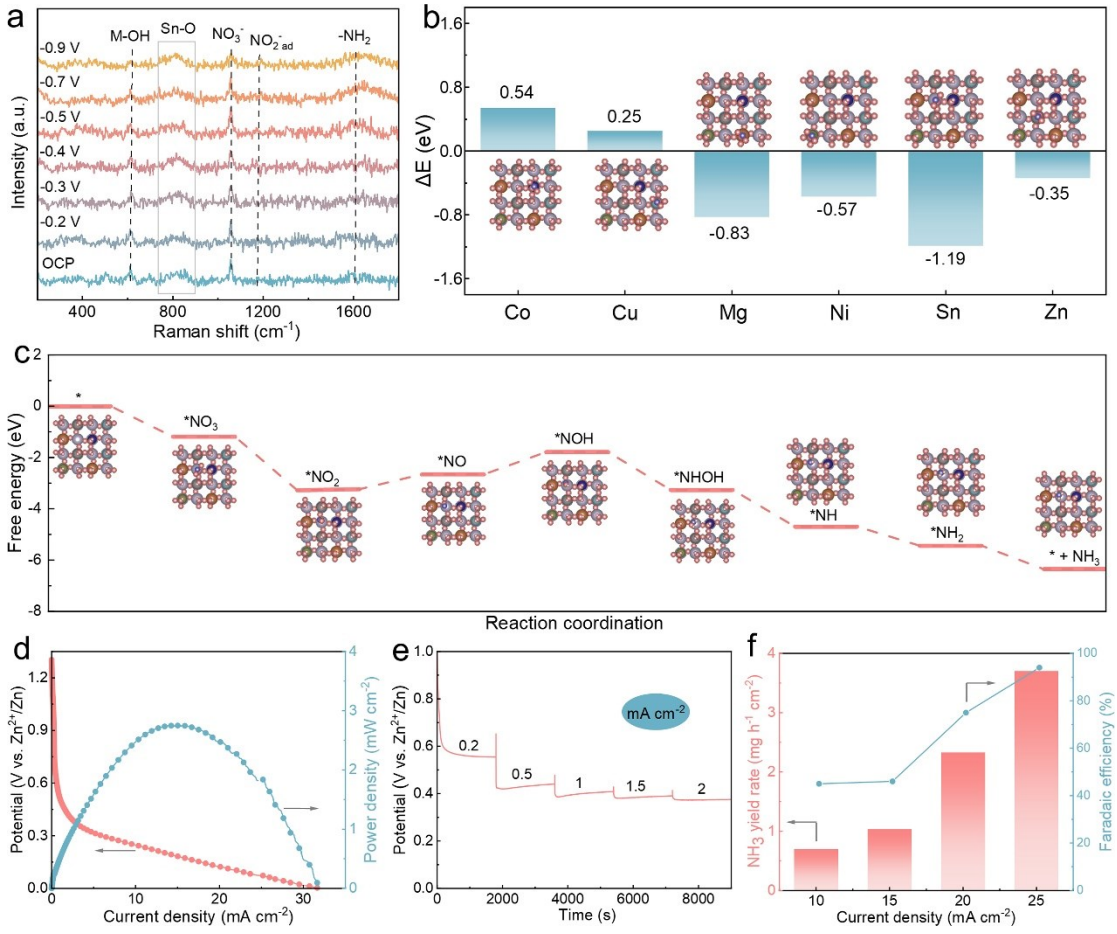


**Figure 5.** a) *In situ* electrochemical Raman spectra. b) The adsorption of the $NO_3^-$ on different sites of HEPH-2 model. c) Free energy diagram for eNRA over HEPH-2. d) Polarization and power density curves for Zn-$NO_3^-$ battery. e) Discharging tests at various current densities, and f) $NH_3$ yield rates and corresponding FE values at various current densities of the Zn-$NO_3^-$ battery with the HEPH-2 catalyst as a cathode.

## 3. Conclusion

In summary, we developed a facile polymer-mediated confined assembly strategy to synthesize nanocubic HEPHs controllably. The optimized HEPH-2, with its larger

electrochemically active surface area and well-exposed active sites, demonstrates superior electrocatalytic performance for eNRA, achieving an impressive $NH_3$ yield rate of 9.28 mg $h^{-1}$ $mg^{-1}_{cat.}$, a high FE of 90.06%. DFT calculations reveal that Sn atoms act as the dominant active centers, providing the strongest $NO_3^-$ adsorption affinity, while the hydrogenation of *NO to *NOH is identified as the potential-determining step. These insights clarify the mechanistic origin of the high activity and highlight how entropy-driven electronic modulation can optimize the balance between adsorption strength and reaction kinetics. Meanwhile, by using HEPH-2 as the cathode to construct a Zn-$NO_3^-$ battery system, the system exhibits a high $NH_3$ yield rate (3.70 mg $h^{-1}$ $cm^{-2}$) and a high FE value (94.21%). This work not only provides a scalable synthesis strategy but also paves the way for designing advanced HEMs for efficient electrocatalytic applications, including sustainable ammonia production and environmental remediation.

## 4. Experimental Section

HEPH samples were prepared using a PVP-assisted nucleation approach. Initially, 10 mmol of $SnCl_4 \cdot 5H_2O$ was dissolved in an aqueous solution with varying PVP concentrations (0%, 5%, 10%), designated as solution A. Meanwhile, 10 mmol of a mixture of metal salts (2 mmol each of $CuAc_2$, $MgAc_2 \cdot 4H_2O$, $CoAc_2 \cdot 4H_2O$, $ZnAc_2 \cdot 2H_2O$, and $NiAc_2 \cdot 4H_2O$) was dissolved in the PVP-containing solution, labeled as solution B. Both solutions were heated to boiling, after which solution B was gradually dripped into solution A. Following this, 2 M NaOH was swiftly introduced into the combined mixture at 100 °C in a water bath. The resulting black precipitate was aged for 4 h to ensure uniform particle size distribution. The solid product was isolated via high-speed centrifugation at 10000 rpm and thoroughly rinsed with deionized water and anhydrous ethanol to remove any residual PVP and impurities. The final products, labeled HEPH-0, HEPH-1, and HEPH-2, were obtained after vacuum drying at 60 °C for 20 h, corresponding to PVP concentrations of 0%, 5%, and 10%, respectively.

## Supporting Information

Supporting Information is available from the Wiley Online Library or from the author.

## Acknowledgements

This work was supported by the National Natural Science Foundation of China (No. 12411530102, No. 52303151) and the Royal Society (IEC\NSFC\233810).

Received: ((will be filled in by the editorial staff))
Revised: ((will be filled in by the editorial staff))
Published online: ((will be filled in by the editorial staff))

**Conflict of Interest**

The authors declare no conflict of interest.

**Reference**

[1] a) G. Soloveichik, *Nat. Catal.* **2019**, 2, 377; b) B. H. R. Suryanto, H.-L. Du, D. Wang, J. Chen, A. N. Simonov, D. R. MacFarlane, *Nat. Catal.* **2019**, 2, 290; c) X. Zhang, Y. Wang, C. Liu, Y. Yu, S. Lu, B. Zhang, *Chem. Eng. J.* **2021**, 403, 126269; d) W. Chen, X. Yang, T. Huang, Y. Li, X. Ren, S. Ye, Q. Zhang, J. Liu, *Compos. Commun.* **2023**, 43, 101715; e) L. Liu, H. Dong, S. Huang, N. Gao, L. Zhang, L.-M. Yang, J. Ba, J. Hofkens, M. Antonietti, T. Liu, F. Lai, Z. Tian, *Sci. China Mater.* **2025**, 68, 472; f) Y. Qie, J. Gao, S. Li, M. Cui, X. Mao, X. Wang, B. Zhang, S. Chi, Y. Jia, Q.-H. Yang, C. Yang, Z. Weng, *Sci. China Mater.* **2024**, 67, 2941.

[2] a) B. H. R. Suryanto, K. Matuszek, J. Choi, R. Y. Hodgetts, H.-L. Du, J. M. Bakker, C. S. M. Kang, P. V. Cherepanov, A. N. Simonov, D. R. MacFarlane, *Science* **2021**, 372, 1187; b) M. Xu, F. Xu, K. Zhu, X. Xu, P. Deng, W. Wu, W. Ye, Z. Sun, P. Gao, *Compos. Commun.* **2022**, 29, 101037; c) J. Wang, L. Yu, L. Hu, G. Chen, H. Xin, X. Feng, *Nat. Commun.* **2018**, 9, 1795; d) X. Wu, A. Ma, D. Liu, X. Li, Y. Zhou, A. T. Kuvarega, B. B. Mamba, H. Li, J. Gui, *Sci. China Mater.* **2023**, 66, 4367.

[3] a) A. Paliwal, C. D. Bandas, E. S. Thornburg, R. T. Haasch, A. A. Gewirth, *ACS Catal.* **2023**, 13, 6754; b) N. R. Singstock, C. B. Musgrave, *J. Am. Chem. Soc.* **2022**, 144, 12800; c) T. Jin, X. Sang, R. R. Unocic, R. T. Kinch, X. Liu, J. Hu, H. Liu, S. Dai, *Adv. Mater.* **2018**, 30, 1707512; d) Y. Zhong, H. Xiong, J. Low, R. Long, Y. Xiong, *eScience* **2023**, 3, 100086.

[4] a) K. Chu, F. Liu, J. Zhu, H. Fu, H. Zhu, Y. Zhu, Y. Zhang, F. Lai, T. Liu, *Adv. Energy Mater.* **2021**, 11, 2003799; b) Y. Wang, C. Wang, M. Li, Y. Yu, B. Zhang, *Chem. Soc. Rev.* **2021**, 50, 6720; c) T. Zhang, W. Zong, Y. Ouyang, Y. Wu, Y.-E. Miao, T. Liu, *Adv. Fiber Mater.* **2021**, 3, 229.

[5] a) Y. Wang, L. Zhang, Y. Niu, D. Fang, J. Wang, Q. Su, C. Wang, *Green Chem.* **2021**, 23, 7594; b) K. Hadjiivanov, H. Knözinger, *Phys. Chem. Chem. Phys.* **2000**, 2, 2803.

[6] a) A. Bhatnagar, M. Sillanpää, *Chem. Eng. J.* **2011**, 168, 493; b) K. Chu, W. Zong, G. Xue, H. Guo, J. Qin, H. Zhu, N. Zhang, Z. Tian, H. Dong, Y.-E. Miao, M. B. J. Roeffaers, J. Hofkens, F. Lai, T. Liu, *J. Am. Chem. Soc.* **2023**, 145, 21387.

[7] a) T. Wang, H. Chen, Z. Yang, J. Liang, S. Dai, *J. Am. Chem. Soc.* **2020**, 142,

4550; b) E. Castle, T. Csanádi, S. Grasso, J. Dusza, M. Reece, *Sci. Rep.* **2018**, 8, 8609; c) H. Chen, K. Jie, C. J. Jafta, Z. Yang, S. Yao, M. Liu, Z. Zhang, J. Liu, M. Chi, J. Fu, S. Dai, *Appl. Catal. B Environ.* **2020**, 276, 119155; d) H. Qiao, X. Wang, Q. Dong, H. Zheng, G. Chen, M. Hong, C.-P. Yang, M. Wu, K. He, L. Hu, *Nano Energy* **2021**, 86, 106029; e) S. Huang, H. Wu, Y. Chen, Z. Zhao, X. Liu, Y. Deng, H. Zhu, *Compos. Commun.* **2023**, 38, 101510; f) H. Guo, Z. Guo, K. Chu, W. Zong, H. Zhu, L. Zhang, C. Liu, T. Liu, J. Hofkens, F. Lai, *Adv. Funct. Mater.* **2023**, 33, 2308229.

[8] a) T. Wang, J. Fan, C. L. Do-Thanh, X. Suo, Z. Yang, H. Chen, Y. Yuan, H. Lyu, S. Yang, S. Dai, *Angew. Chem. Int. Ed.* **2021**, 60, 9953; b) M. Chen, N. Kitiphatpiboon, C. Feng, A. Abudula, Y. Ma, G. Guan, *eScience* **2023**, 3, 100111; c) Y. Lu, Z. Li, G. Zhang, H. Zhang, D. Fan, M. Zhao, H. Zhu, X. Yang, *Adv. Fiber Mater.* **2025**, 7, 563.

[9] D. Chen, M. Qiao, Y. R. Lu, L. Hao, D. Liu, C. L. Dong, Y. Li, S. Wang, *Angew. Chem. Int. Ed.* **2018**, 57, 8691.

[10] Y. Zhou, L. Zhang, M. Wang, X. Shen, Z. Zhu, T. Qian, C. Yan, J. Lu, *Nat. Commun.* **2025**, 16, 7915.

[11] a) D. Kim, Y. J. Lee, K. H. Ahn, *Compos. Commun.* **2022**, 30, 101093; b) T. Wan, C. Lv, K. Ye, W. Weng, W. Xiao, *Sci. China Mater.* **2025**, DOI: 10.1007/s40843-025-3519-0; c) J. Zhang, P. Du, X. Li, W. Liu, C. Li, Y. Ji, C. Zeng, D. Zong, Z. Cai, *Adv. Fiber Mater.* **2025**, DOI: 10.1007/s42765-025-00602-0.

[12] S. Mei, B. Xiang, S. Guo, J. Deng, J. Fu, X. Zhang, Y. Zheng, B. Gao, K. Huo, P. K. Chu, *Adv. Funct. Mater.* **2023**, 34, 2301217.

[13] a) X. He, T. Xie, K. Dong, J. Nan, H. Sun, Y. Yao, X. Fan, D. Zheng, Y. Luo, S. Sun, Q. Liu, L. Li, W. Chu, L. Xie, Q. Kong, X. Sun, *Sci. China Mater.* **2024**, 68, 2756; b) L. Qin, Y. Liu, S. Zhu, D. Wu, G. Wang, J. Zhang, Y. Wang, L. Hou, C. Yuan, *J. Mater. Chem. A* **2021**, 9, 20405; c) S. Guddehalli Chandrappa, P. Moni, D. Chen, G. Karkera, K. R. Prakasha, R. A. Caruso, A. S. Prakash, *ACS Appl. Energy Mater.* **2021**, 4, 13425.

[14] a) S. Dong, A. Niu, K. Wang, P. Hu, H. Guo, S. Sun, Y. Luo, Q. Liu, X. Sun, T. Li, *Appl. Catal. B Environ.* **2023**, 333, 122772; b) Y. Wang, Y. Kang, Y. Miao, M. Jia, S. Long, L. Diao, L. Zhang, D. Li, G. Wu, *Compos. Commun.* **2024**, 48, 101890; c) Y. Wang, N. Li, H. Liu, J. Shi, Y. Li, X. Wu, Z. Wang, C. Huang, K. Chen, D. Zhang, T. Wu, P. Li, C. Liu, L. Mi, *Adv. Fiber Mater.* **2023**, 5, 2002.

[15] N. Li, X. Li, W. Zhang, Y. Du, *J. Alloys Compd.* **2020**, 831, 154764.

[16] Q.-M. Sun, W.-G. Zhong, Y.-X. Liu, H. Wang, Y.-L. Zhai, J.-S. Wang, X. Ao, K.-Z. Li, Z.-S. Li, C.-D. Wang, *Rare Met.* **2025**, 44, 4724.

[17] C. Liu, X. R. Shi, K. Yue, P. Wang, K. Zhan, X. Wang, B. Y. Xia, Y. Yan, *Adv. Mater.* **2023**, 35, 2211177.

[18] H. Guo, Z. Guo, G. Xue, H. Wang, J. Gong, K. Chu, J. Qin, Y. Guan, H. Dong, Y. Chen, Y. E. Miao, C. Zhang, H. Liu, T. Liu, J. Hofkens, F. Lai, *Adv. Mater.* **2025**, 37, 2500224.

[19] Y. Wan, M. Pei, Y. Tang, Y. Liu, W. Yan, J. Zhang, R. Lv, *Adv. Mater.* **2025**, 37,

2417696.
[20] S.-N. Zhang, P. Gao, Q.-Y. Liu, Z. Zhang, B.-L. Leng, J.-S. Chen, X.-H. Li, *Nat. Commun.* **2024**, 15, 10877.
[21] H. Guo, Y. Zhou, K. Chu, X. Cao, J. Qin, N. Zhang, M. B. J. Roeffaers, R. Zboril, J. Hofkens, K. Mullen, F. Lai, T. Liu, *J. Am. Chem. Soc.* **2025**, 147, 3119.

A polyvinylpyrrolidone-mediated confined assembly strategy enables the synthesis of nanocubic high-entropy perovskite hydroxides with optimized active site exposure, achieving efficient ammonia production and high energy performance in the Zn-$NO_3^-$ battery.

Keywords: high-entropy perovskite hydroxides, electrocatalytic nitrate reduction, polymer-mediated confined assembly, ammonia production, zinc-nitrate battery

Chaofan Liu†, Tian Xie†, Guohao Xue†, Xiaobo Xu, Hele Guo*, Yawen Guan, Tianlu Wang, Ziyuan Rao, Nan Zhang, Tianxi Liu, Claire J. Carmalt, Johan Hofkens, Xiaoqin Zeng and Feili Lai*

**Polymer-mediated confined assembly of high-entropy perovskite hydroxide nanocubes for ammonia production and zinc–nitrate battery energy supply**